PHYSICAL PROPERTIES OF THE SUPERCONDUCTING, TOPOLOGICAL TERNARY CHALCOGENIDE FAMILY $[Tl_4](Sn_xTl_{1-x})Te_3$

by

Benjamin D. Wasser

A thesis submitted to Johns Hopkins University in conformity with the requirements for the degree of Master of Science and Engineering

Baltimore, Maryland

May, 2014

ABSTRACT

It has been recently discovered that the perovskite superconductor Tl_5Te_3 and its tin-doped derivative, $[Tl_4](Tl_{0.4}Sn_{0.6})Te_3$ have topologically protected metallic surface states. However, when Tl_5Te_3 is fully doped with tin, the system is predicted by Density Functional Theory (DFT) to be without surface states. This implies that there exists a topological transition determined by amount of tin that is doped in the system. Here we report the physical properties of the $[Tl_4](Sn_xTl_{1-x})Te_3$ family of materials. Structurally, a symmetry lowering distortion occurs when tin and thallium order on the perovskite "B" site, causing a loss of the 4-fold axis and tetragonal symmetry of the parent I4/mcm space group. This structural transition coincides with the loss of superconductivity around x=0.5. The large superconducting fraction of Tl_5Te_3, the superconducting dome, and the strong Sn composition-property coupling, make $[Tl_4](Tl_{0.4}Sn_{0.6})Te_3$ an ideal platform in which to probe the topological phase transition in a superconductor.

ACKNOWLEDGEMENTS

I'd like to start by thanking my Masters advisor, Dr. Tyrel McQueen, for all of his assistance and tutelage. He was always willing to make time for my work and the work of my colleagues to provide wisdom and support when I encountered difficulty with an experiment or understanding a topic I am very grateful that he accepted me as one of his graduate students.

I also received advice and assistance from my peers, the other members of the McQueen research group. Kate Arpino, David Wallace, John Sheckelton, Ben Trump, Adam Phelan, Allyson Fry, Patrick Cottingham, Zach Kelly, and Jessica Panella were all indispensible to my growth, teaching me a tremendous amount about inorganic chemistry and research methodology.

Aside from my Masters studies, I wanted to thank Professor Kevin Hemker and the Hemker research group for my introduction into scientific research. Particularly Betsy Congdon and the Solar Probe Plus team at the Civilian Space Division of the Johns Hopkins University Applied Physics Laboratory for trusting me with testing the thermal protection system and inviting me to continue to work on the project throughout my undergraduate career. Those experiences has truly

exposed me to amazing opportunities and undoubtedly without her, I would never have discovered my love for space and space technology.

All my undergraduate friends deserve recognition, for learning and growing with me, shaping me academically as well as socially. I was extremely lucky to meet my greatest friends the moment I arrived at JHU. Thank you Jorge, Ian, Chris, Sarah, Carolyn, Dan, Elliot, Senam, Gabo, Corey and all the other amazing people in my life. Thanks to Kimber for giving me a reason to stay on task, I don't think I would have gotten it done in time without her.

There are countless people I would love to thank, my inspiring high school teachers, Dr. Gershman and Mr. Kutch for believing that I could achieve great things, and convincing me of the same. I am incredibly grateful to my robotics team, my fencing team, and all of my friends who have helped me along my way.

Most important of all, I would like to thank my family. My Father, my Mother, my sister Rebecca, my sister Sarah are the most important people in the world to me. I love them; they are my inspiration and my driving force, always pushing me to be better than the best I can be. Nobody will understand what it means to be a part of my family, but they should be extremely. I dedicate this work to them, if they ever read it, I will quiz them after.

TABLE OF CONTENTS

LIST OF TABLES

LIST OF FIGURES

CHAPTER 1: INTRODUCTION & BACKGROUND

The compound of interest in this thesis is the tin doped chalcogenide superconductor Tl_5Te_3 and the family of materials in the $[Tl_4](Tl_{1-x}Sn_x)Te_3$ series. The primary objective of this study is to study the structural, electronic, and thermal properties of this series in an attempt to understand the phase transition that occurs between the topological superconductor (x=0), the topological insulator (x=0.6), and a trivial insulator (x=1)

1.1 MOTIVATION AND FOCUS OF RESEARCH

The Band Theory of Solids distinguishes four major categories of materials based on their electronic transport properties [1]. These categories are distinguished from each other by the difference in energies between the highest energy state, known as the conduction band, and the lowest energy state, known as the valence band. When there is no difference and therefore no separation between the conduction and valence band, the material is a metal. A small overlap between the conduction and valence band is known as a semimetal. This separation, known as a band gap, is very small for the class of material known as semiconductors. The electronic state of semiconductors can easily be altered so the material becomes conducting. Insulators have a large band gap and require a sizable amount of energy in order to excite an electron.

The differences between these three material classes are illustrated in Fig. 1.1.

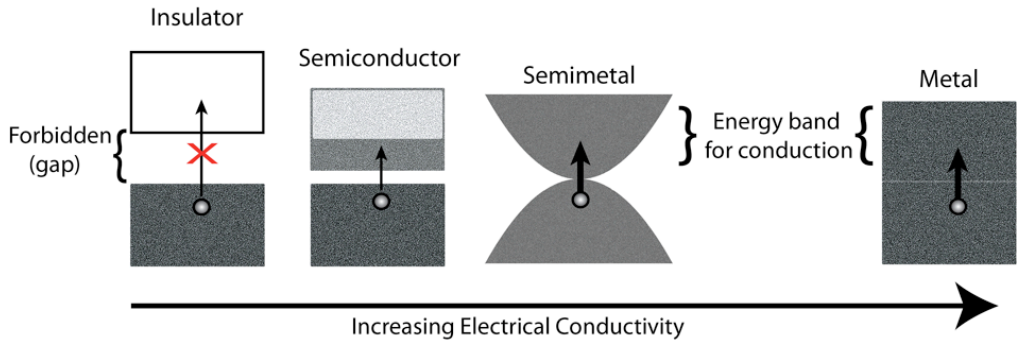

Figure 1.1: Illustration of the Band Theory of Solids and the four classical categories of electronic materials.

Recently, a new addition to the Band Theory of Solids that focuses on the topological order of the material as well as its electronic transport properties has been devised [2,3]. Two systems that are in the same topological class can be simply deformed to resemble the other. The topological order of an object is dependant wholly on its genus, i.e. the number of holes in the object. Applying these topological laws to the Band Theory of Solids, one would assume that all materials with a band gap (semiconductors and insulators) would be in the same topological class. However, insulating materials have been discovered for which their band structure cannot be deformed in a smooth continuous manner to resemble a trivial insulator [4,5]. This new class of materials, which was

predicted in 2005 and experimentally confirmed shortly after, is known as Topological Insulators (TIs) [4,6,7,8].

TIs have attracted a considerable amount of attention from many different fields and industries. The non-trivial topology has a profound impact of the physical properties of the material. The bulk of the material is an insulator, however, the surface supports conducting states, restricting the path of any applied current to the exterior of a three dimensional Tl [9]. Even more interesting perhaps, is that this current is spin polarized [10]. The potential application of TIs to spintronics is highly anticipated.

In 2008, it was theorized that the interface of a topological insulator and a superconductor could possibly test an as of yet undiscovered subatomic particle, the Majorana fermion [11,12]. This particle is unique in that the antiparticle of a Majorana fermion is another Majorana fermion. The Majorana fermion is ideal for future quantum computing systems, as they are fault-tolerant and immune to decoherence [13]. It has been attempted to create the Majorana fermion by physically bringing a superconductor and a TI together and by doping but this limits studies to small samples and low volume fraction superconductivity. Currently, the Majorana fermion has not been directly observed [14].

The goal then becomes to find a material that hosts topological surface states as well as superconductivity. Such a material, known as a topological superconductor (TS), would be the ideal platform to search for Majorana fermions and to build new devices exploring what effects the exotic particle exhibits. This material would have a robust superconducting volume fraction. Studying the physical properties of a material family that contains both a superconductor and a topological insulator and determining the process by which the material transitions from one state to the other will illuminate the underpinnings of the topological phase transition and provide a future framework on which to search for other TSs.

1.2 SYNTHESIS METHODS

Polycrystalline samples of $[Tl_4](Tl_{1-x}Sn_x)Te_3$ were prepared by heating elemental Tl (Strem Chemicals, 99.9%, **warning: toxic, carcinogenic**) and Te (Alfa Aesar, 99.999+%) and Sn (NOAH Technologies, 99.9%) in a vacuum sealed silica ampoule to 550˚C and held for 24 hours, then stepped down to 350˚C and held again for 24 hours. The ampoule was then quenched in water back down to room temperature. Elemental Thallium was handled in an inert environment to prevent oxidation. Compositions of single crystals were assumed to be

homogenous with the bulk sample. The bulk sample composition was determined by Rietveld refinements of X-ray diffraction data.

1.3 THESIS OVERVIEW

The key focuses of this study is to determine the electronic, structural, and thermal properties of the $[Tl_4](Tl_{1-x}Sn_x)Te_3$ family of materials their relation to the topological protected transition, as well as the composition range of superconductivity and TIs within the series.

Chapter 2 discusses the structural properties of the series, using well-documented methods, which includes laboratory X-ray diffraction (XRD) supplemented with high-resolution synchrotron x-ray data (SXRD). This chapter proves that full doping (x=1) can be achieved in this material family and determines the evolution of the lattice parameters across the series. The material's potential space group and its implication on band structure are discussed.

Chapter 3 deals exclusively on the electronic properties of the series, where the methods, data, and results of both magnetization and resistivity data are mentioned. The theories behind the magnetization and superconductivity are explained and an estimate for T_c, the superconducting transition temperature is determined for each member in the series. Chapter 4 handles the thermal properties, but more specifically the heat capacity. A semi-adiabatic heat pulse method is

used to obtain the heat capacity data, and the analysis to determine the electronic contribution to heat capacity as well as an equal entropy estimate for T_c are summarized.

Chapter 5 attempts to combine the results and data collected on the physical properties of the material family to determine the topological phase transition and the possibility of more topological superconductors within the series. The implication of the results and suggestion for future work are also presented.

CHAPTER 2: DETERMINATION OF STRUCTURE

The $[Tl_4]MTe_3$ (M=Sn, Pb, Bi, Sb, La, Nd, and Mo) family of materials are reported to have a tetragonal perovskite structure [15,16]. X-ray diffraction was used to verify the synthesis method and composition of the $[Tl_4](Sn_xTl_{1-x})Te_3$ products. Previous synchrotron diffraction data and literature have been interpreted to mean that that the maximum tin content is either x=0.6 or 0.8 [16] XRD analysis has revealed a slight deviation from Vegard's Law, but the continuous change in lattice parameters implies that it is possible to create a series from $0 \leq x \leq 1$. Upon further analysis we have also found that the space group for the $[Tl_4](Sn_xTl_{1-x})Te_3$ family is more likely Cmcm or Cmma then the previously reported I4/mcm for x>0.

2.1 BASIC PRINCIPLES OF X-RAY DIFFRACTION

Bragg's law states that different crystalline layers will diffract X-rays is specific directions,

$$n\lambda = 2d\sin\theta \tag{2.1}$$

where n is an integer, λ is the wavelength of the incident beam of x-rays, d is the spacing between atomic lattice planes, and θ is the angle between the incident beam and the lattice planes. X-ray beams will elastically scatter electrons from the atoms of a crystal. Only in certain

directions, as described by the aforementioned equation, will the scattered waves constructively interfere, which causes XRD peaks, also known as reflections. These reflections are specific to the composition and crystal structure of a given material, and through further analysis the positions can reveal unit cell parameters and the space group of the crystal.

High resolution X-rays can be produced in a synchrotron radiation source. A synchrotron accelerates charged particles radially, most often by strong magnetic fields. The particles eventually reach near relativistic speeds and produce very intense and highly collimated radiation. These x-rays can be used to gather diffraction data at an unparalleled resolution. All synchrotron x-ray diffraction data in this thesis was gathered at the 11-BM beamline powder diffraction instrument run by the Advanced Photon Source at the Argonne National Laboratory.

2.3 DETERMINATION OF LATTICE PARAMETERS

Using the previously mentioned synthesis method, samples of $[Tl_4](Sn_xTl_{1-x})Te_3$, where $0 \leq x \leq 1.3$. The products were crushed into a powder and mixed with a small amount of Molybdenum (Alfa Aesar, 99.95%) for use as a standard for lattice parameter determination using TOPAS software for diffraction data. As expected, as more tin is substituted for thallium the lattice parameters change. As shown in

Figure 2.3 there is an increase in the c lattice parameter and a corresponding decrease in the a and b parameter, which can be attributed to the smaller Sn atoms substituting Tl on the Perovskite B site.

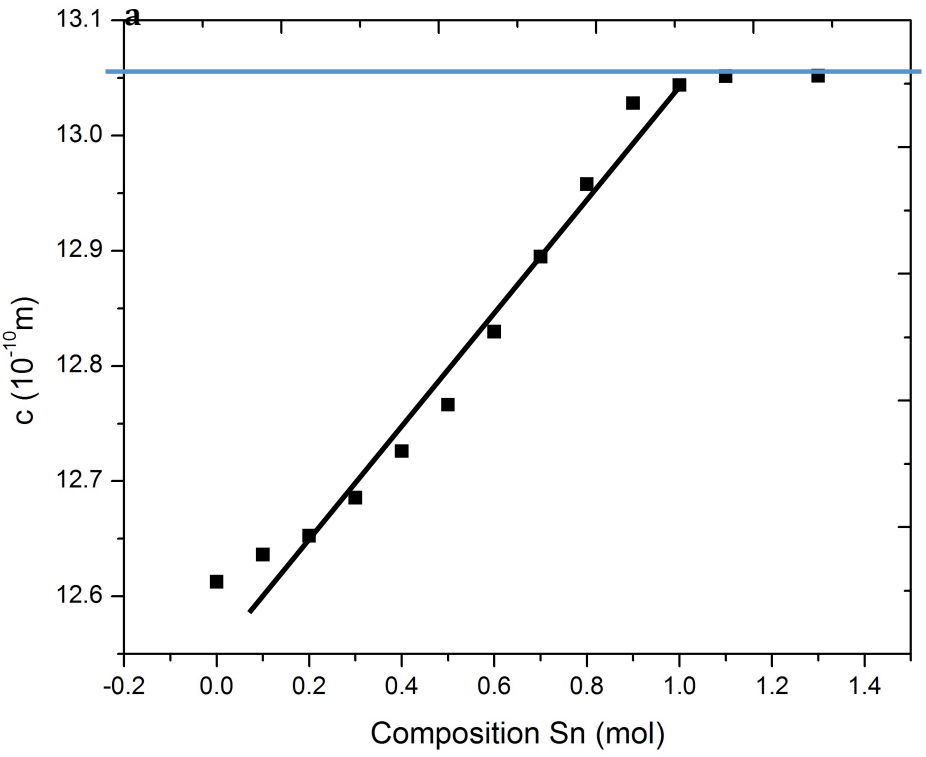

Figure 2.1: a) Lattice parameter c with varying tin composition. b) Lattice parameter a with varying tin composition. The lattice parameter deviates from Vegard's law slightly, which means the alloy's parameters can be determined by linear interpolation. The horizontal line represents the region where no significant changes in lattice parameter occur.

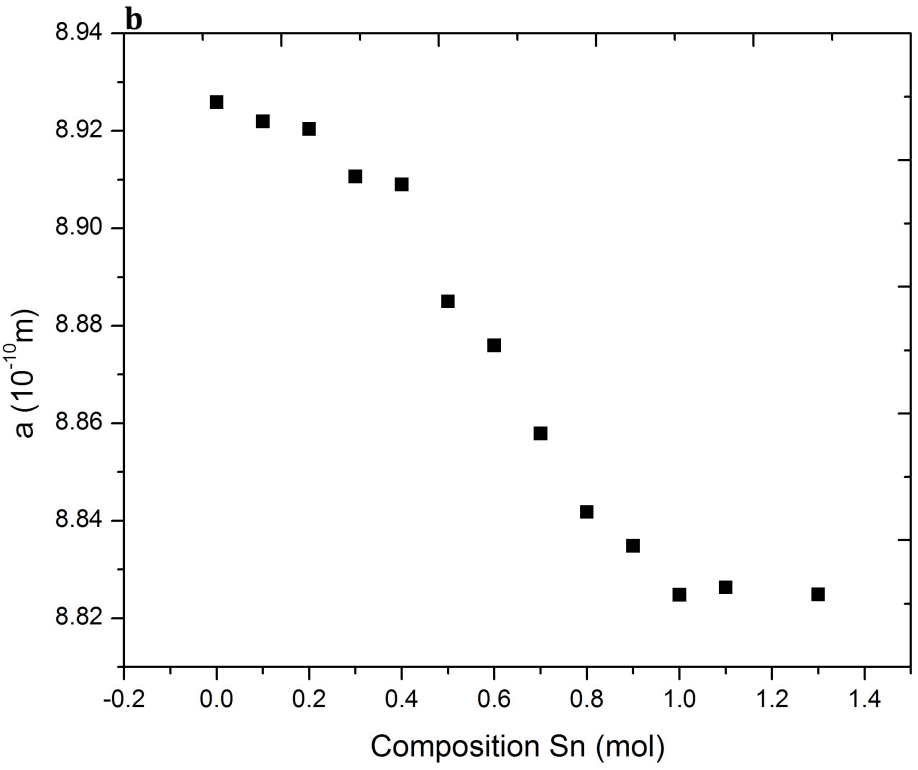

Samples with a Sn composition above x=1 produce secondary phases in X-ray diffraction data, and no longer exhibits any significant change in lattice parameters, implying that x=1 is likely the solubility limit of Tin in $[Tl_4](Sn_xTl_{1-x})Te_3$. This is consistent with the assumption that the Tin is substitution for Thallium solely on the perovskite "B" site. Table 2.2 contains all the lattice parameters for products in the series. These 2.5 g of each sample were produced in lab using high purity elements. The samples listed in the table were used for every measurement in this thesis.

Composition Sn	c (angstroms)	a (angstoms)	c/a
0	12.612(8)	8.925(8)	1.4130(6)
0.1	12.636(1)	8.921(9)	1.4163(0)
0.2	12.652(7)	8.920(3)	1.4184(1)
0.3	12.685(6)	8.910(6)	1.4236(5)
0.4	12.726(0)	8.908(9)	1.4284(5)
0.5	12.766(4)	8.885(0)	1.4368(5)
0.6	12.829(7)	8.875(9)	1.4454(4)
0.7	12.894(8)	8.857(8)	1.4557(4)
0.8	12.957(8)	8.841(8)	1.4655(1)
0.9	13.028(2)	8.834(8)	1.4746(3)
1	13.043(9)	8.824(7)	1.4780(9)

Table 2.2: Lattice parameters for each member of the $[Tl_4](Sn_xTl_{1-x})Te_3$ series

2.2 SPACE GROUP AND CRYSTAL SYMMETRY

In previous literature, Tl_5Te_3 is described as having an I4/mcm space group. This space group describes a tetragonal perovskite structure (ABX_3), with a network of corner sharing $TlTe_6$ (BX octahedra occupied by $[Tl_4]$ (A) tetraheda. An example of a Tl_5Te_3 unit cell can be seen in Figure 2.2a. The reported structure for $SnTl_4Te_3$ is the same as its parent compound, with an 8.82 x 8.82 x 13.03 Å unit cell [17]. However, using high-resolution synchrotron x-ray diffraction, additional peak splitting indicate a lowering of symmetry to at least orthorhombic become visible. Peak splitting of the reflections are prominently displayed when compared to the high-resolution diffraction data of the parent

compound. Examples of this obvious breaking of symmetry are shown in Figure 2.3.

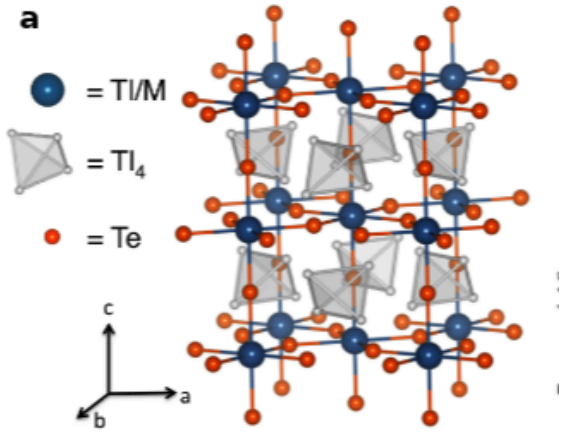

Figure 2.2: a) Unit cell of $[Tl_4](M/Tl)Te_3$ in the I4/mcm space group. b) unit cell of $[Tl_4](M/Tl)Te_3$ in the Cmcm space group.

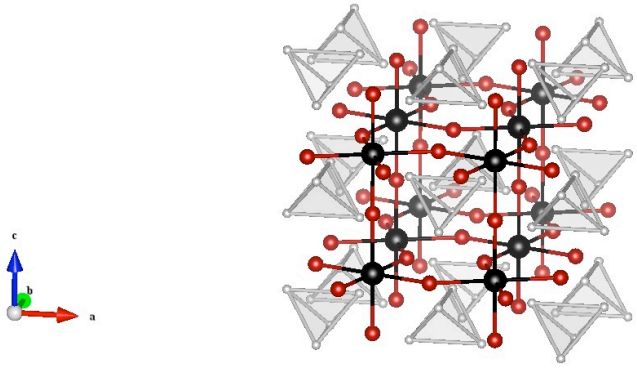

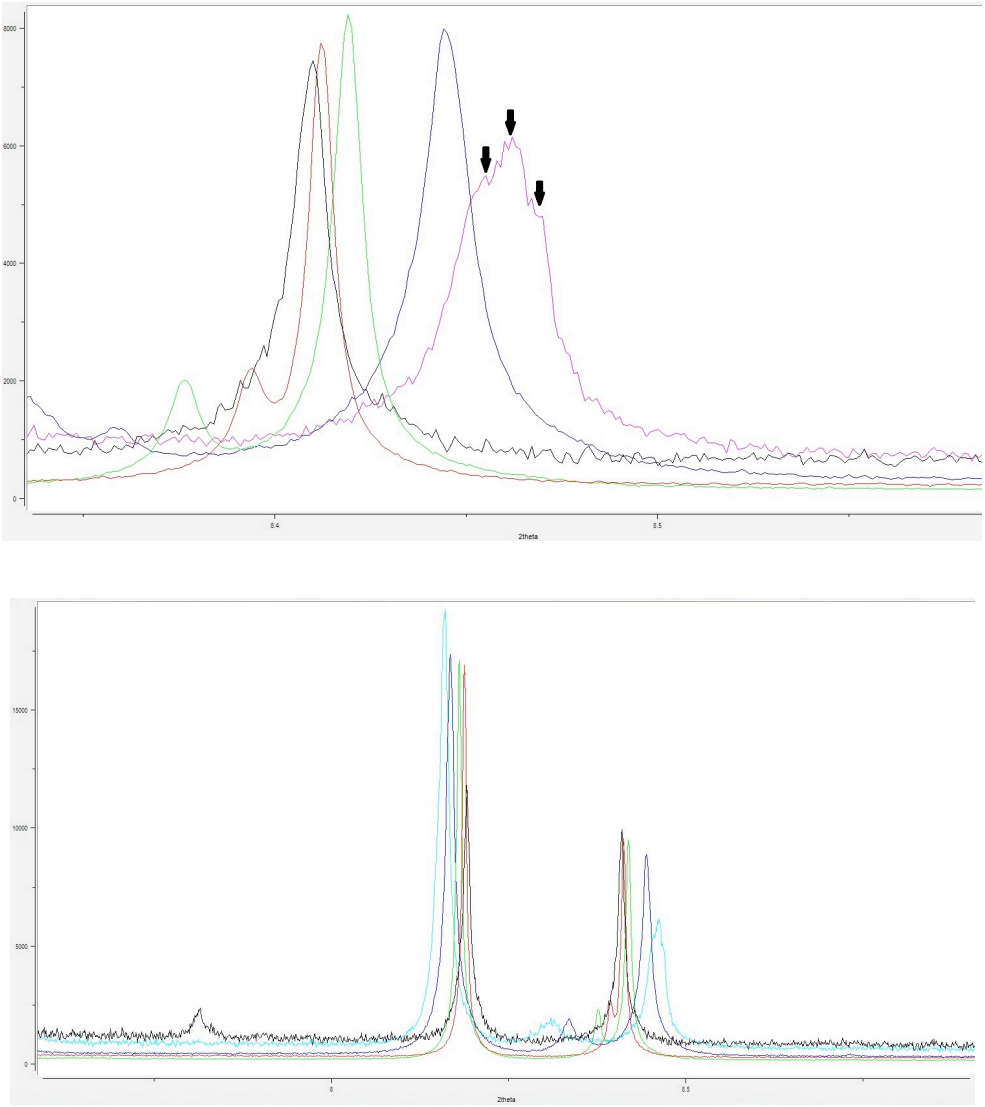

Figure 2.3: examples of peak splitting and peak shifting in $[Tl_4](Sn_xTl_{1-x})Te_3$ series with increasing Sn content.

Both peak splitting and peak shifting gives reason to explore space groups with lower crystal symmetry.

Assuming that the tin will substitute on the perovskite “B” site due to the strong interactions of the bonded $[Tl_4]$ tetrahedra, chart detailing a list of potential space groups was created. This taxonomy is shown in Figure 2.4. Each branch off of the parent space group represents a loss of symmetry due to a particular ordering in the crystal. First, a splitting of the perovskite “B” site, with a 4c Wyckoff position in the parent space group I4/mcm, for any potential Tin-Thallium ordering was considered. This ordering has 5 possibilities, rock salt, layers parallel and perpendicular to the “c” axis, and columns both parallel and perpendicular. The next level of ordering reflects the possible charge disproportionation of thallium into Tl^{1+} and Tl^{3+}, which causes a further splitting of the “B” site. A third ordering, not shown in Figure 2.4, is caused by a displacement due to lone pair interactions from the tin. This ordering would cause any Sn special positions to move to a more general location, further reducing its symmetry. This diagram maps out the sources of distortions, attempts to match potential space groups to those sources, or any combination therein, and allows a systematic approach to determining the space group of the $[Tl_4](Sn_xTl_{1-x})Te_3$ family.

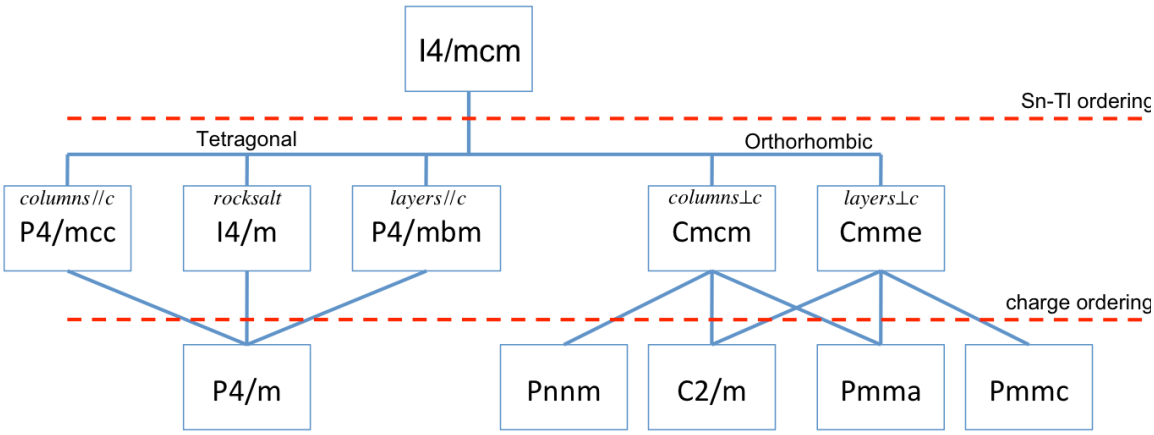

Figure 2.4: Taxonomy of potential space group distortions. The parent space group I4/mcm can be potentially distorted via Sn-Tl ordering on the perovskite "B" site. Further distortions can becaused by charge disproportionation of the thallium into Tl^{1+} and Tl^{3+}, or displacement of Sn from the ideal site (not shown)

Indexing the peaks of the SXRD data on Topas software suggested either the Fmmm and Ibam space groups, both of which are maximal isomorphic subgroups of the parent I4/mcm structure, but more specifically reflect a non-tetragonal symmetry. Using this information, in conjunction with the taxonomy created in Figure 2.4 refinements were made to the Cmcm and Cmma space groups. Both the Cmma and Cmcm are maximal isomorphic subgroups of the Fmmm, which in turn is a subgroup of the parent compound's crystal symmetry I4/mcm. The lattice parameters, ^{2}, and R-factors for each space group are presented in Table 2.1. Increasing the number of free parameters will always

improve the fit, which is reflected in Table 2.1 as the lower symmetry space groups show small improvements. The Cmcm is almost statistically identical to the Cmma space group, an example of the $SnTl_4Te_3$ with the Cmcm crystal structure is shown in Figure 2.2b.

Space Group	I4/mcm	Cmma	Cmcm
a (Angstroms)	8.869(4)	12.543(6)	12.543(6)
b (Angstroms)	8.869(4)	12.747(9)	12.543(0)
c (Angstroms)	12.747(9)	12.543(0)	12.747(9)
Volume	1002.84(6)	2005.71(2)	2005.71(8)
Z	16	32	32
X^2	5.1984	4.41	4.41
R_{Bragg}	4.48	4.47	4.47
R_p	6.75	6.39	6.37
R_{wp}	10.19	9.42	9.39

Table 2.1: Refinement details for $[Tl_4](Sn_{0.5}Tl_{0.5})Te_3$ in the I4/mcm, Cmcm, and Cmma space groups.

The Cmcm space group is an orthorhombic distortion of I4/mcm. Specifically it contains an in phase rotation of the octahedra about the "b" axis, with columns of Sn/Tl sites that are perpendicular to the "c" axis. The Cmcm phase sometimes appears as an intermediate step as I4/mcm distorts to Pnma [18]. Experimentally however, this phase isn't always present in every system with this structural transformation.

CHAPTER 3: ELECTRONIC PROPERTIES

The electronic properties of the $[Tl_4](Sn_xTl_{1-x})Te_3$ family of materials is explored in the following chapter. The resistivity of the series, only reported through personal correspondence in previous literature, is determined by four-probe resistivity measurements. The AC magnetic susceptibility (ACMS) of the series is also explored, primarily to determine whether or not the product is a superconductor and to get a rough estimate of T_c. The ACMS data will also be used in a later chapter in an attempt to elucidate the presence of topologically protected surface states. The four-probe and ACMS measurement procedures are explained in full and the results across the series are compared.

3.1 AC MAGNETIC SUSCEPTIBILITY THEORY

AC magnetization susceptibility (ACMS) measurements provide information about the magnetization dynamics within a sample of material. The sample is placed under a DC field, with a small AC drive magnetic field superimposed. This induces a time dependant moment,

$$M_{AC} = \left(\frac{dM}{dH}\right) \cdot H_{AC} \sin(\omega t) \qquad 3.1$$

Where H_{AC} is the amplitude of the AC driving field, $\left(\frac{dM}{dH}\right)$ is the slope of the magnetization curve (also known as χ, the susceptibility), and ω is

the frequency of the driving field. Superconductors, due to the Meissner effect, become superdiamagnetic, meaning that the magnetic field inside the material is almost zero, and therefore the susceptibility, $\chi' = -1$.

3.2 AC-MAGNETIC SUSCEPTIBILITY RESULTS

All AMCS measurements were taken on a Quantum Design, Inc. Physical Properties Measurement System (PPMS). Powders of $[Tl_4](Sn_xTl_{1-x})Te_3$ samples with masses ~100mg were prepared by being wrapped tightly in saran-wrap and placed into a non-magnetic plastic sample straw and then placed in the PPMS. The measurements were taken in zero applied dc field and from T=300K to T=1.8K. The ACMS results for samples with varying tin content are shown in Figure 3.1.

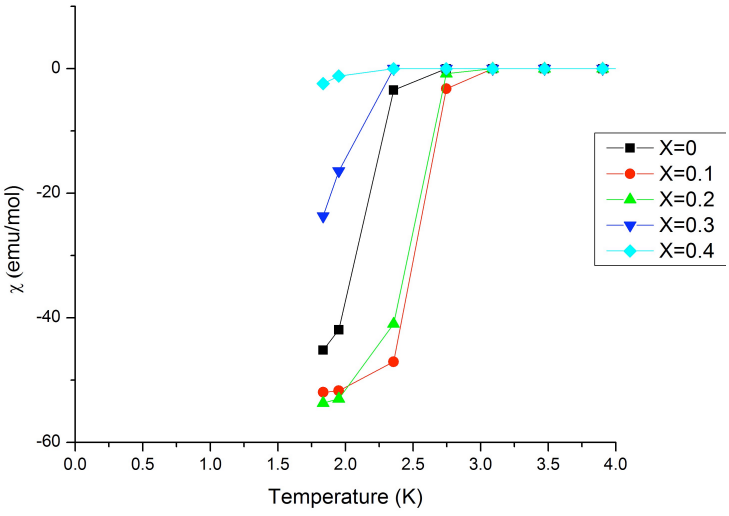

Figure 3.1: AC-susceptibility measurements for 0≤x≤.4

Apparent in the data is a superconducting transition occurs at low temperatures in samples with small amounts of tin doping. This transition occurs at increasingly higher temperature until it ultimately becomes suppressed at $[Tl_4](Sn_{0.4}Tl_{0.6})Te_3$. Taking the midpoint of non-zero values for χ as an estimate for the superconducting transition temperature, T_c, we can see how this transition varies with increasing tin content as shown in Figure 3.2. A slight superconducting dome occurs from $0 \leq x \leq 0.3$ before the transition is suppressed completely. Superconductivity is suppressed in the same range of x where the additional states are related to the structural distortion caused by Sn-Tl ordering. The degree on non-tetragonality is also depicted in Figure 3.2. The distortion may reach a maximum or minimum value at an intermediate doping, which would correspond to a maximum value of T_c. Future work must be undertaken to truly elucidate the structure-property relationship in $[Tl_4](Sn_xTl_{1-x})Te_3$

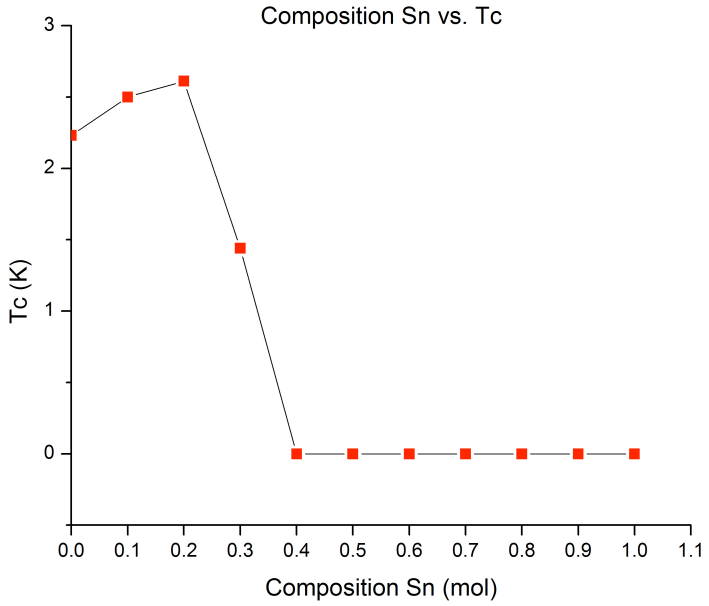

Figure 3.2: T_c vs composition Sn from AC magnetic susceptibility measurements. The superconducting dome is apparent in the low-doped regime.

3.3 INTRODUCTION TO 4-PROBE MEASUREMENT

The resistance of a material can provide information about a material's band structure as well as determine if there are any electronic transitions occurring with varying temperature [19]. Finding the resistance of a material is a common characterization tool used in solid-state physics, as it is helpful in determining the number of electronic carriers available for conduction. The resistance of a material is dependant wholly upon the geometry of the sample and an intrinsic property known as resistivity,

$$\rho = \frac{A}{l} R \qquad 3.2$$

where A is the cross sectional area of the sample, l is the sample length, R is resistance, and ρ is the resistivity. In order to find the resistivity of a sample, the four-point probe resistance measurement option was used for the Quantum Design, Inc. Physical Properties Measurement System. Four electrical contacts, made from thin Pt wire, are adhered to the surface of a sample via quick drying silver paste. Current is passed through the outer leads while the two inner leads measure the drop in voltage. The contact geometry schematic is shown in Figure 3.3.

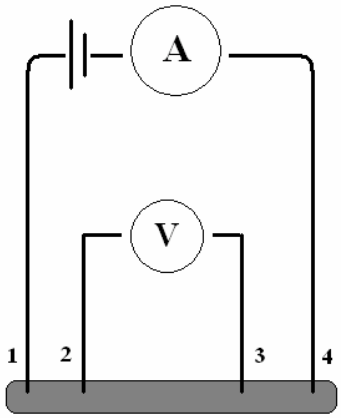

Figure 3.3: General schematic for a four-point probe resistance measurement

For a four-point probe resistance measurement, l becomes the length between the two inner leads, yet this distance is often hard to ascertain systematically due to spreading of the silver paste contacts. Additionally,

because $[Tl_4](Sn_xTl_{1-x})Te_3$ does not cleave neatly, surfaces were prepared by mechanically polishing a flat plane from polycrystalline samples with 60 and then 150 grit sandpaper. This process may have introduced micro-cracks, which can potentially influence resistance measurements, therefore the error in the geometrical factor can be on the order of 10% and the resistivity data should be considered with this in mind.

3.4 RESISTIVITY OF $[Tl_4](Sn_xTl_{1-x})Te_3$

Resistivity measurements were performed on samples in the $[Tl_4](Sn_xTl_{1-x})Te_3$ family are reported in figure 3.4. The sharp drop in resistivity for many samples at low temperature is due to the superconducting transition. The resistivity varies slightly in magnitude with the amount of tin doping, but no overarching trend is made apparent. Looking at Figure 3.4, it is apparent that the resistivities of the samples exhibit prototypical metallic temperature response with a superconducting transition below T_c. X=1 appears to be an intrinsic semi-conductor and x=0.5 a metal. This data is in agreement with previously reported results.

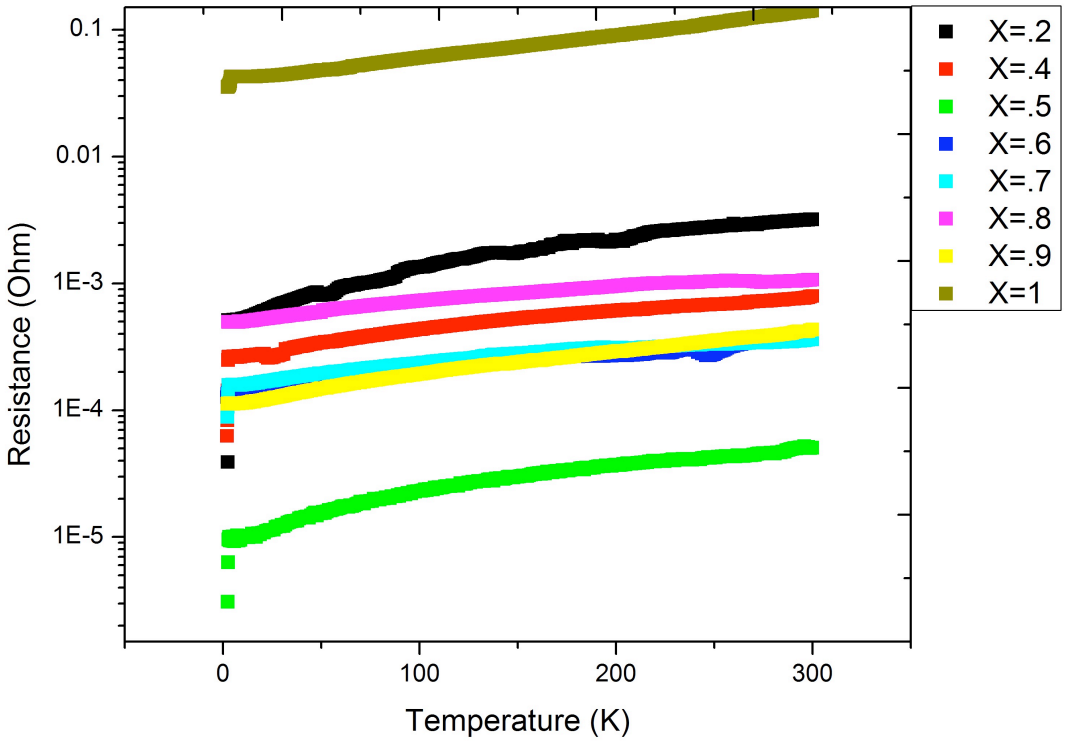

Figure 3.4: Normalized resistivity measurements using four-probe sensing.

CHAPTER 4: THERMAL PROPERTIES

4.1 SEMI-ADIABATIC CALORIMETRY

The low temperature heat capacities of the samples were measured on the Quantum Design, Inc. PPMS heat capacity option using a semi-adiabatic thermal relaxation technique. A small polycrystalline sample with a mass ~ 10 mg is set on a stage using Apiezon N grease to ensure a proper thermal contact with the stage. The PPMS measures the heat capacity at constant pressure, C_p, by releasing a controlled heat pulse to the sample and records the differences in temperature between the sample and the puck upon heating and cooling.

The sample is assumed to be in poor thermal contact with its surroundings, but it also assumes zero contributions to the heat capacity from both the stage and the grease. As such, an addenda measurement is made and then subtracted from the signal to give the heat capacity of the sample alone. Three separate measurements were made, each with varying applied fields ($\mu_0 H$=0,1,5 T) in order to determine the electronic contribution to heat capacity for each sample. The field was oriented at a random angle in relation to the crystal axis depending on the orientation of the polycrystalline sample to the stage. An example of C_p data is presented in Figure 4.1 for the parent compound Tl_5Te_3. The total heat capacity quickly reaches a maximum value of 3R per atom, as described

by the Dulong-Petite model of heat capacity. The Debye temperature, the temperature of the material's highest normal mode of vibration, is approximately 170°K [20]

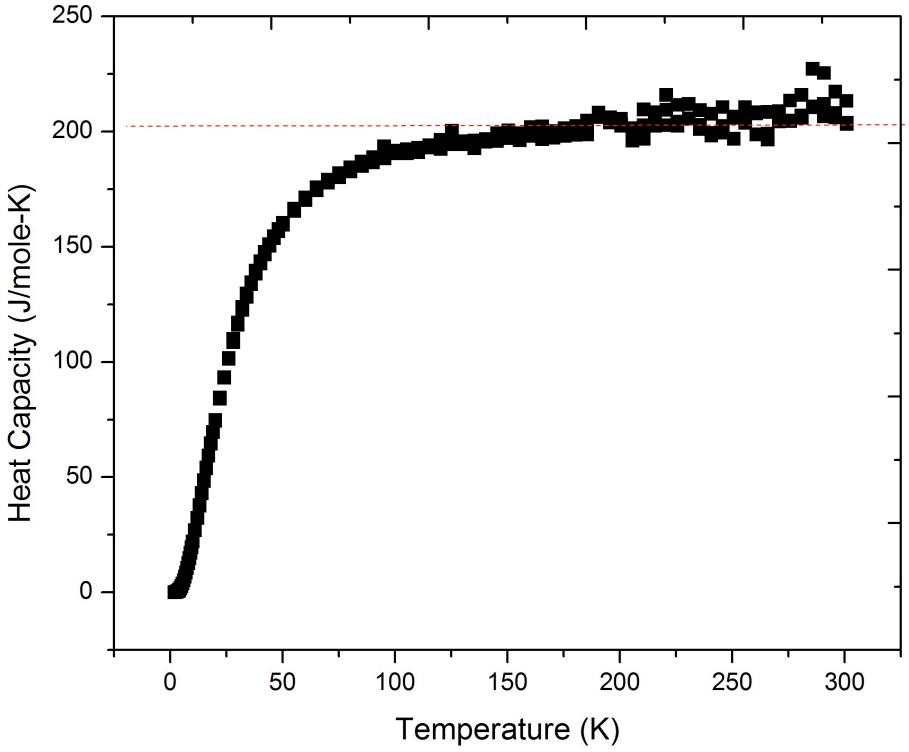

Figure 4.1: Heat Capacity Data for Tl_5Te_3, the Dulong-Petit limit is marked by a horizontal dotted line.

A plot of C_p/T^3 is a useful tool to isolate specific phonon contributions to specific heat. Debye modes, which are strongly dispersed phonon branches, appear as plateaus in the low temperature regime, whereas

Einstein modes are seen as local maxima. Such a plot is shown in Figure 4.2

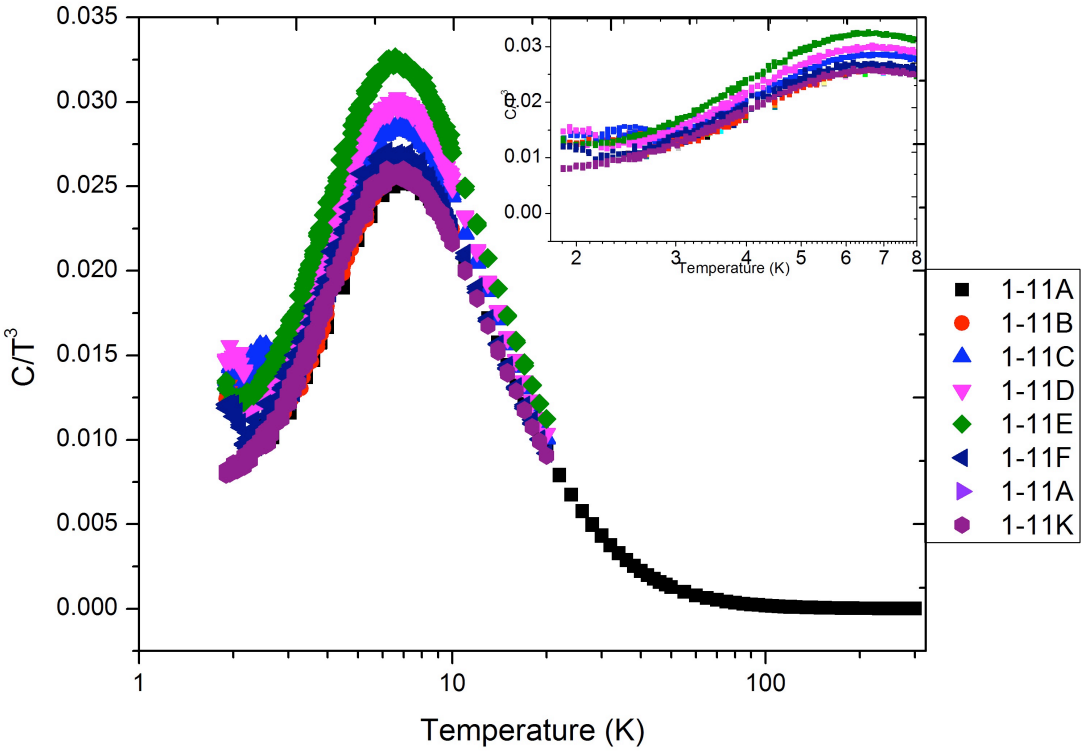

Figure 4.2: Local phonon modes in Tl_5Te_3. The local maximum indicates the presence of a weakly dispersing phonon mode

4.2 HEAT CAPACITY ANALYSIS

A simple analysis method for low T specific heat assumes that there are two sources that contribute to the overall specific heat, coming

from the phonon lattice vibrations as well as a contribution from electrons.

$$\frac{C_P}{T} = \gamma + \left(\beta_3 T^2 + \beta_5 T^4\right) \qquad 4.1$$

Where in the equation γ, β_3, β_5 are all constants. The constant γ is the electronic component to specific heat, and the remaining terms are due to lattice vibrations. Normally, the highest term is ignored, but because $\frac{\theta_D}{50} \approx 3K$ and the fits were performed up 20K it was necessary to include.

Equation 4.1 is fit to each sample's C_p measurement with an applied field of 5T. We assume the magnetic field will suppress any superconducting transition and provide a normal state estimate for the heat capacity of each sample. The phonon contribution from the 5T heat capacity data is then subtracted from the heat capacity vs temperature data for both the 0 and 1 Tesla data in order to isolate the electronic contribution to the heat capacity.

$$\frac{C_{electronic}}{T} = \frac{C_p}{T} - \left(\beta_3 T^2 + \beta_5 T^4\right)_{H=5T} \qquad 4.2$$

The superconducting transition increases the electronic contribution, creating a feature in C_p data around T_c known as the λ anomaly, a phase transition. The electronic contribution for $[Tl_4](Sn_{0.2}Tl_{0.8})Te_3$ with a visible λ anomaly is visible as an upturn in the data in Figure 4.2. The

electronic contribution can also be used to find the change in entropy, $Q = \frac{\Delta C}{T_c}$, associated with the superconducting transition by applying an equal entropy construction. This construction demonstrated in Figure 4.3, and is also useful in determining the precise location of the transition temperature, T_c. The parameters and values $Q, \gamma, \beta_3, \beta_5, T_c$ are contained in table 4.1

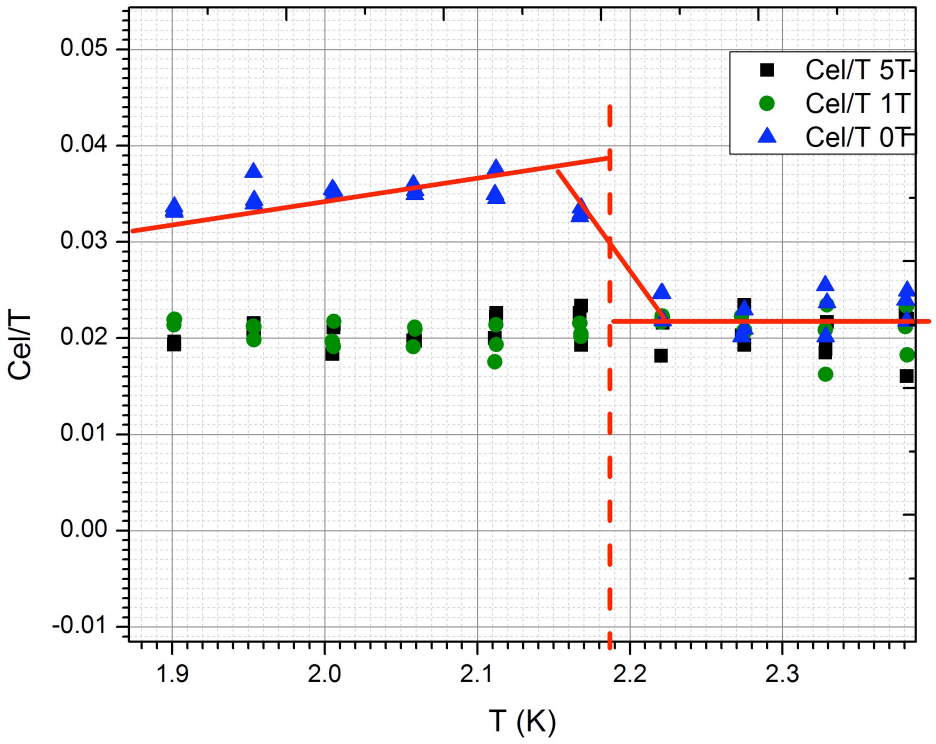

Figure 4.3: Electronic contribution to heat capacity for $[Tl_4](Sn_{0.4}Tl_{0.6})Te_3$ the equal entropy construction allows for a more accurate prediction to the superconducting transition temperature and an estimate for the change in entropy associated with the transition.

X	0	0.1	0.2	0.3	0.4	0.5	0.6	0.7	0.8	0.9	1
gamma	0.009	0.008	0.012	0.01204	0.00587	0.00201					5.64E-03
B3	0.006	0.00465	0.00439	0.00335	0.00555	0.00463					0.00222
B5	----	7.89E-04	9.70E-04	1.12E-03	1.13E-03	9.12E-04					1.06E-03
Cp	0.012	0.011	0.01	0.009	0.0025	0	0	0	0	0	0
Tc	2.03	2.74	2.78	2.19	1.915	0	0	0	0	0	0.00E+00
C/gTc	1.333333	1.375	0.833333	0.747508	0.425894	0	0	0	0	0	0

Table 4.1: Heat capacity parameters for $0 \leq x \leq .5$

CHAPTER 5: CONCLUSIONS

5.1 SUMMARY OF RESEARCH

The members of series $[Tl_4](Sn_xTl_{1-x})Te_3$ are superconducting from $0 \leq x \leq 0.4$ but otherwise displays a typical metallic response. The superconducting transition is strongly coupled with the material's crystal structure and symmetry. This structure-property relation, in conjunction with the appearance of topologically protected states at x=1 makes the $[Tl_4](Sn_xTl_{1-x})Te_3$ series an ideal candidate to study the presence of a topological phase transition. It is hoped that further studies on this family of materials will lead to the development of new physics and a framework to search for future topological superconductors.

Prior to the start of the work described in this thesis, only basic studies on the electronic properties of Tl_5Te_3 and its tin-doped derivative $SnTl_4Te_3$. Only until recently with the discovery of the presence of topologically protected states did the material return back to limelight as a potential topological superconductor. A single sample of $SnTl_4Te_3$ was subjected to high resolution synchrotron x-rays and reitveld refinements were made assuming the space group of I4/mcm. Specific heat, resistivity, and magnetization measurements were taken on samples of Tl_5Te_3.

The X-ray diffraction data reveled that the space group of $[Tl_4](Sn_xTl_{1-x})Te_3$ is in fact not I4/mcm, but much more likely orthorhombic due to lattice distortions from tin ordering. Refinements suggest the actual space group to be Cmma or Cmcm. This distortion can be potentially linked to the superconducting properties of the material, and why it is suppressed or even the topologically protected surface states. The orthorhombic distortion explains why previous literature believed the maximum amount of tin allowed in the series was either x=0.6 or 0.8, when in fact 1 mol of Thallium can be substituted completely for 1 mol of Tin. AC magnetic susceptibility tests reveal that there is a superconducting dome present, and samples of $[Tl_4](Sn_xTl_{1-x})Te_3$ between x=0 and x=0.5 are all low temperature superconductors. It is hoped that this material will provide insight into the relationship between superconductivity and topologically protected states.

5.2 FUTURE WORK

It is possible that the orthorhombic distortion suppresses the mechanism that causes superconductivity in Tl_5Te_3 and it has yet to be determined whether there is a structural relationship to the topological properties of the material. Determining the presence of topological protected states in the $[Tl_4](Sn_xTl_{1-x})Te_3$ series would allow deductions to be made about the topological phase transition that is assumed to occur

somewhere in between the full doped $SnTl_4Te_3$ and the parent compound, Tl_5Te_3. Neutron powder diffraction or single crystal x-ray diffraction could aid in the determination of the material's space group. Knowing the crystal symmetry may provide some clues as to the structure-property relationship. Understanding this phenomenon will allow for a greater understanding of topological phase transitions as well as provide a potential framework for discovering other materials with similar properties.

BIBLIOGRAPHY

[1] F. Bloch, Über die Quantenmechanik der Elektronen in Kristallgittern, Zeits. f. Physik 52 (1928), 555–600.

[2] X.-G. Wen, Topological orders and edge excitations in fractional quantum hall states, Adv. Phys. 44 (1995), 405–473.

[3] D. J. Thouless, M. Kohmoto, M. P. Nightingale, and M. den Nijs, Quantized Hall conductance in a two-dimensional periodic potential, Phys. Rev. Lett. 49 (1982), 405–408.

[4] C. L. Kane and E. J. Mele, Z2 Topological Order and the Quantum Spin Hall Effect, Phys. Rev. Lett. 95 (2005), 146802.

[5] Y. Xia, D. Qian, D. Hsieh, L. Wray, A. Pal, H. Lin, A. Bansil, D. Grauer, Y. S. Hor, R. J. Cava, and M. Z. Hasan, Observation of a large-gap topological-insulator class with a single Dirac cone on the surface, Nature Phys. 5 (2009), 398–402.

[6] C. L. Kane and E. J. Mele, Quantum Spin Hall Effect in Graphene, Phys. Rev. Lett. 95 (2005), 226801.

[7] B. A. Bernevig, T. L. Hughes, and S.-C. Zhang, Quantum spin Hal l effect and topological phase transition in HgTe quantum wells., Science 314 (2006), 1757–1761.

[8] M. König, S. Wiedmann, C. Brüne, A. Roth, H. Buhmann, L. W. Molenkamp, X.-L. Qi, and S.-C. Zhang, Quantum Spin Hall Insulator State in HgTe Quantum Wells, Science 318 (2007), 766–770.

[9] L. Fu and C. L. Kane, Topological insulators with inversion symmetry Phys. Rev. B 76 (2007), 045302.

[10] D. Hsieh, Y. Xia, L. Wray, D. Qian, A. Pal, J. H. Dil, J. Osterwalder, F. Meier, G. Bihlmayer, C. L. Kane, Y. S. Hor, R. J. Cava, and M. Z. Hasan, Observation of unconventional quantum spin textures in topological insulators, Science 323 (2009), 919–922.

[11] Sau, J. D., Lutchyn, R. M., Tewari, S. & Das Sarma, S. Robustness of Ma jorana fermions in proximity-induced superconductors. Phys. Rev. B 82, 094522 (2010).

[12] Potter, A. C. & Lee, P. A. Topological superconductivity and Majorana fermions in metallic surface states. Phys. Rev. B 85, 094516

(2012).

[13] Linder, J., Tanaka, Y., Yokoyama, T., Sudbo, A. & Nagaosa, N. Unconventional Superconductivity on a Topological Superconductor Phys. Rev. Lett. 104, 067001 (2010).

[14] Mourik, V, Zuo, K and Frolov, SM et al. Signatures of Majorana fermions in hybrid superconductor-superconductor nanowire devices. Science 2012; 336: 1003–7.

[15] Bottcher, P., Doert, T., Druska, C., & Bradtmoller, S. Investigations on compounds with Cr5B3 and In5Bi3 structure types, J. Alloys Comp. 246, 209-215 (1997).

[16] Glazer, A. M. The Classification of Tilted Octahedra in Perovskites. Acta Cryst. B 28, 3384-3392 (1972).

[17] Arpino, K.E., Wallace, D.C., et al. Topological Surface States in $[Tl_4](Sn_xTl_{1-x})Te_3$ arXiv:1303.6350 [cond-mat.mtrl-sci]

[18] Rajan, R. Subtle distortions in some dielectric perovskites, J. Indian Inst. Sci. 88:2, 2008

[19] L. B. Valdes: “Resistivity Measurements on Germanium for Transistors,” Proceedings of the IRE 42 (1954) 2:420

[20] Tari, A. The Specific Heat of Matter at Low Temperatures. (Imperial College Press, London, UK, 2003).